Title

Electrochemical and Structural Investigation of the Mechanism of Irreversibility in Li3V2(PO4)3 Cathodes

Journal

The Journal of Physical Chemistry C, 120(13)

ISSN

1932-7447

Authors

Kim, Soojeong
Zhang, Zhengxi
Wang, Senlin
et al.

Publication Date

2016-04-07

DOI

10.1021/acs.jpcc.6b00408

Peer reviewed

THE JOURNAL OF PHYSICAL CHEMISTRY

Article

Electrochemical and Structural Investigation of the Mechanism of Irreversibility in LiV(PO) Cathodes

Soojeong Kim, Zhengxi Zhang, Senlin Wang, Li Yang,
Elton J. Cairns, James E Penner-Hahn, and Aniruddha Deb

J. Phys. Chem. C, **Just Accepted Manuscript** • DOI: 10.1021/acs.jpcc.6b00408 • Publication Date (Web): 11 Mar 2016

Electrochemical and Structural Investigation of the Mechanism of Irreversibility in $Li_3V_2(PO_4)_3$ Cathodes

Soojeong Kim,[a] Zhengxi Zhang,[b] Senlin Wang,[b] Li Yang,[b] Elton J. Cairns,[c] James E Penner-Hahn,[a] and Aniruddha Deb*[a]*

[a] Dr. Soojeong Kim, Prof. James E Penner-Hahn, Dr. Aniruddha Deb, Department of Chemistry, University of Michigan, Ann Arbor, MI 48109, United States. [b] Dr. Zhengxi Zhang, Dr. Senlin Wang, Prof. Li Yang, School of Chemistry and Chemical Technology, Shanghai Jiao Tong University, Shanghai 200240, PR China. [c] Prof. Elton J. Cairns, Environmental Energy Technologies Division, Lawrence Berkeley National Laboratory, Berkeley, California 94720, and Chemical and Biomolecular Engineering Department, University of California, Berkeley, 94720, United States.

ABSTRACT Lithium-ion batteries dominate the battery field, particularly for electric and hybrid vehicles. Monoclinic $Li_3V_2(PO_4)_3$ has emerged as one of the most promising candidates for the cathode in lithium-ion batteries, offering better environmental safety and lower cost than competing materials. We have used *in situ* x-ray absorption spectroscopy to characterize the evolution of the vanadium in a $Li_3V_2(PO_4)_3$ cathode as it is cycled electrochemically. These data demonstrate the presence of significant kinetic effects such that the measured electrochemical behavior does not represent the bulk vanadium. When the cell is cycled between 3 and 4.5 V, there are two distinct vanadium species. When the potential is raised above 4.5 V a third species is observed, consistent with formation of V^{5+}. XANES data for the cathode after 3-4.8 V cycling are consistent with a severely distorted vanadium site, suggesting that lithium-vanadium anti-site mixing may be responsible for the electrochemical irreversibility that is seen above 4.5 V.

Introduction

Electrochemical devices are the most promising of the available alternative energy storage technologies, due to their flexibility, high efficiency in energy conversion and minimal maintenance. However, it is becoming increasingly clear that the energy economy needs higher-performance, lower cost, safer energy storage systems for both stationary energy storage for the electrical grid and mobile energy storage for electric and hybrid vehicles. There have been many reports of fires involving oxide-based lithium ion batteries. The search for safer electrode materials has been a high priority, and phosphate-based electrodes are attractive because, unlike oxide materials, they do not release oxygen. In this work, we focus on the study of $Li_3V_2(PO_4)_3$ as a new, safer cathode material for lithium ion cells. Through in-depth structural and spectroscopic analyses we characterize the vanadium redox chemistry in $Li_3V_2(PO_4)_3$; this will

aid in the design and development of improved, safer electrode materials for advanced lithium ion batteries.

Among materials with a phosphate polyanion framework, $LiMPO_4$ (M= Co, Mn, Ni, and Fe)[1-4] and $Li_3V_2(PO_4)_3$ (LVP)[5-7] have all shown considerable promise as lithium-ion cathodes. Both systems contain redox active metals and mobile Li ions within a rigid phosphate framework, and both show good electrochemical capacities and stability. The monoclinic $Li_3V_2(PO_4)_3$ system and its doped variants show excellent promise as high potential cathode materials because of their high reversible capacity, high operating potential (~4 V), good ion mobility, improved safety characteristics, and low environmental impact.[6-8] All three lithium ions can be deintercalated giving a high theoretical capacity of 197 mAh g^{-1}.[8-15] In order to understand the functioning of LVP at the atomic level we have measured *in situ* x-ray absorption spectroscopy (XAS) during charge and discharge under different conditions. These data allow us to directly correlate average vanadium oxidation state with electrochemical potential, and to characterize at the atomic level the mechanism for high-potential inactivation.

Experimental

Preparation of $Li_3V_2(PO_4)_3$/C composite and electrode. LVP composite electrodes were prepared using hexanedioic acid ($C_6H_{10}O_4$) as the chelating agent, where V_2O_5 and oxalic acid in stoichiometric ratio of 1:3 were dissolved in deionized water and then stirred at 70°C. With the formation of a blue solution, a stoichiometric mixture of $NH_4H_2PO_4$, Li_2CO_3, and $C_6H_{10}O_4$ were added. This was followed by a 4 hour stirring in an air oven at 100°C, when a gel was formed. The gel was then heated to a temperature of 350°C for 4 hours, in the presence of a nitrogen atmosphere to allow NH_3 and H_2O to escape. Finally the resultant product was heated at 750°C for another 4 hours in the presence of nitrogen. X-ray powder diffraction (XRD) measurements

(Figure S1, lower panel) were conducted by a Rigaku D/max-2200/PC diffractometer. The as-prepared material was in the monoclinic phase with the space group of $P2_1/n$, and the unit cell parameters were, a=8.608(3), b=8.553(6), c=12.060(3), and β=90.363(5). The morphology was analyzed by field emitting scanning electron microscopy (FE-SEM, JEOL JSM-7401F)[16]. The data (Figure S1) show that the particles of the sample merge with each other and form a porous network. This microstructure is beneficial for the electrolyte to penetrate with the positive materials, which helps for good electronic contact among the composites particles.

In situ XANES and EXAFS. The electrochemical XAS reaction cell was assembled in an argon-filled glove box. The glass wool separator was punched to give a disk with an outer diameter of 20 mm and inner diameter of 6 mm. The separator was placed on top of the electrode $Li_3V_2(PO_4)_3$/C (x=0) soaked in 1 M $LiPF_6$ electrolyte, dissolved in 50 wt % ethylene carbonate (EC) and 50 wt % dimethylcarbonate (DMC) obtained as a solution from BASF. Finally, a lithium foil counter-electrode was punched to give a disk with an outer diameter of 14 mm and an inner diameter of 8 mm and placed on top of the separator which was soaked with electrolyte. Kapton film (25.4 μm thickness) was utilized as the X-ray window for this *in situ* electrochemical reaction cell. More detailed information on the design of this reaction cell can be found in Deb et al.[17]

For the XAS measurements, cycling of the electrochemical reaction cell was done continuously using a Princeton Applied Research VERSASTAT potentiostat, with the XAS data being collected as the electrochemistry proceeded under constant current control. The electrode was cycled at 0.1 C or 0.2 C (1C=140mAh g^{-1}) while XAS scans (~40 minutes each) were recorded continuously. Spectra were measured over a potential range of 3-4.5 or 3-4.8 V, giving between 6 and 20 scans for each charge or discharge cycle. Current flow was terminated when

the threshold potential was reached and several additional XAS scans were recorded while the electrode equilibrated.

In situ XAS measurements were performed in transmission mode at the bending magnet beam line station D of the DND-CAT (Sector 5), at the Advanced Photon Source, using a water cooled Si(111) double crystal monochromator, and the energy resolution of the monochromatic beam was determined to be ~1.0 eV . A beam size of about 0.3×4 mm^2 was used for the beam to pass easily through the *in situ* cell X-ray window resulting in an incident photon flux of ~10^{10} photons/s. X-ray flux before and after the electrode sample was measured using N_2 filled ion chambers. A vanadium foil reference and a third ion chamber were placed behind the sample in order to provide an internal energy reference with the first inflection point of the vanadium foil defined as 5465 eV. The monochromator was scanned from 200 eV below to 800 eV above the vanadium K-absorption edge. Scans were measured using 5 eV steps in the pre-edge region, 0.5 eV steps in the near-edge region and 0.05 $Å^{-1}$ steps in the EXAFS region. The data were integrated for 1 s per step in the pre-edge, 1.5 s per step in the near edge region and 1.5-25 s per step in the EXAFS region for a total scan time of about 40 min. The scans were made continuously as charge/discharge cycling continued. When the potential approached the cut off voltages (3.0V, 4.5V and 4.8V) the electrochemistry was stopped for 1 hour to perform extra scans of the XANES region.

Data Analysis. The XANES data were analyzed using the MBACK program,[18] and the EXAFS data were analyzed using the EXAFSPAK software package.[19] The raw data were first imported in EXAFSPAK to do the EXAFS analysis using FEFF9[20] to calculate *ab-initio* phase and amplitude parameters. A pre-edge background and a cubic spline EXAFS background were subtracted and the EXAFS oscillations were normalized to the appropriate Victoreen function

modeling the absorption decrease above the edge.[21] The resulting $\chi(k)$ function was weighted with k^3 to account for the damping of oscillations with increasing k. The radial structure functions presented here were obtained by Fourier transformation of $k^3\chi(k)$ using a k-range of 1.5–11.5Å^{-1}.

Principal component analysis Principal component analysis was performed separately for each cycle. For each cycle, all of the XANES spectra collected during both charge and discharge were used to determine how many components were necessary for that cycle, using PRESTOPRONTO.[22] The XANES scans for a single charge/discharge cycle were imported for PCA analysis over the energy range of 5455-5525 eV. The eigenvectors were derived from the set of XANES spectra by principal component analysis. These eigenvectors were used to estimate the number of vanadium species present for each cycle using the residual standard deviation (RSD) to evaluate the significance of each added component (Figure S2). Iterative Target Factor Analysis (ITFA)[23] was used to align the components obtained from PCA to the real experimental XANES. The reconstructed experimental spectra are shown in Figure 1. The reconstructed components are qualitatively similar and are broadly reflective of V^{3+} (Component 1) and V^{4+} (Component 2).

The PCA components from ITFA (shown in Figure 1), were used to fit the experimental XANES measured at each state of charge in order to determine the fractional composition of each component. The results of these fits are shown in Figure 2. In addition, the experimental XANES were also fit using authentic V^{3+}, V^{4+} and (for **C** and **D**) V^{5+} models in order to estimate the absolute oxidation state of vanadium. The results of the model fits are shown in Figure S3 for cycles **A** and **B**. Analogous results were obtained for cycles **C** and **D**, but are less well

defined because of the presence of three non-orthogonal reference XANES spectra. All least squares XANES fitting was performed with the program suite SixPack.[24-25]

Near-edge fitting. To characterize the possible change in the coordination and anti-site mixing of the vanadium during cycling, we fitted the XANES region with a pseudo-Voigt function together with an arctan to model the rising edge. A summary of the analysis is shown in the Table S1. In the absence of an authentic model for the putative tetrahedral V^{5+} (see below), it is impossible to reliably estimate the amount of anti-site mixing that might take place. For Cu^{2+}, the change from centrosymmetric to tetrahedral results in an approximately 7-fold increase in intensity. If there were a similar increase here, the putative tetrahedral V^{5+} would have peak area of 882. This is used to give some estimate of the possible extent of anti-site mixing.

Rate Estimation. At the end of each charge (4.5 V and 4.8 V) and discharge cycle (3.0 V), we stopped the electrochemistry and recorded several additional XANES spectra in order to investigate the rate at which the electrode reaches equilibrium. We fitted these XANES spectra in the same way that we fit the XANES data in the PCA analysis (above, and Figure 1). The change in the PCA component in cycle **A**, **B**, with respect to time is shown in Figure S4. If these data are modeled as an exponential approach to equilibrium (not shown), the apparent time constants ranges from 0.022 to 0.082 min^{-1}.

Results

When LVP is cycled from 3-4.5 V (traces **A** and **B** in Figure 3, see also the differential capacity in Figure S5) there are three distinct plateaus at ~3.6 V, 3.7 V and 4.1 V vs. Li/Li^+. These have been attributed to oxidation from V^{3+} to $V^{3.25+}$, from $V^{3.25+}$ to $V^{3.5+}$, and from $V^{3.5+}$ to V^{4+}, respectively.[15-16, 26-36] The existence of three well-defined plateaus demonstrates that oxidation takes place via successive two-phase transitions between 3-4.5 V.[8, 37-39]

The first cycle (**A**) shows significant hysteresis (~25 mAh g^{-1}) and even larger apparent capacity loss (~40 mAh g^{-1}). The second cycle (**B**) at higher rate shows similar behavior, with modest capacity recovery on the charge cycle and somewhat smaller capacity loss on the discharge cycle. As long as the potential is limited to 4.5 V, well defined plateaus are seen on both charge and discharge, demonstrating electrochemical reversibility. However, when the electrode is cycled above 4.5 V (**C** and **D**) no plateaus are observed on discharge. The electrode appears to recover somewhat on sitting at 3 V, since 4 plateaus are again observed on charge cycle **D**. The hysteresis seen in Figure 3, **C** and **D** has been attributed to disruption of vanadium charge ordering in the fully delithiated phase.[8] Intriguingly we also see hysteresis in **A** and **B**, without forming the fully delithiated phase. For the discharge cycles in **C** and **D**, there are no plateaus; this is consistent with previous observations and has been interpreted as evidence for a disordered Li insertion process.[8, 40] The shoulder at 3.3-3.4V in the first charge curve (**A** of Figure 3) suggests that there may be a modification of the local environment of the Li that occurs during the first extraction of Li from the structure. Note that this feature is absent from the subsequent charging curves.

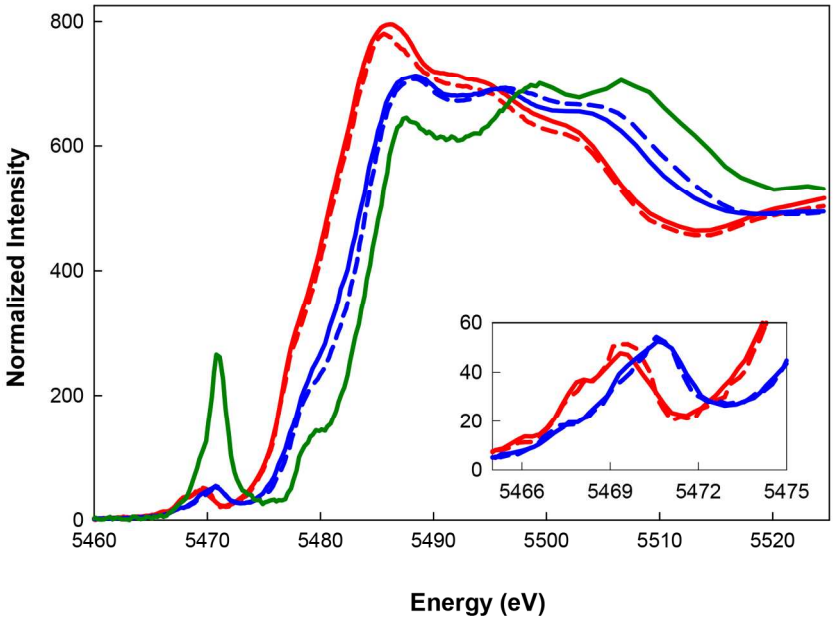

Figure 1. ITFA reconstructed components. Red) Component 1 for **A**, **B**, (solid) and **C**, **D** (dashed); Blue) Component 2 for **A**, **B** (solid) and **C**, **D** (dashed); Green) Component 3 for **C** and **D**

The XANES spectra for cycle **A** are shown in Figure S6. There is a significant shift in the absorption edge to higher energy during charge and a shift back to lower energy during discharge, consistent with formation of V^{4+} and re-reduction to V^{3+}. Similar results are seen for cycles **B**-**D** (Figure S6). The 1s-3d transitions for the spectra in Figure S6 are shown in Figure 4a,b. As with the edge energy, the 1s-3d transition shifts to higher energy on charge and lower energy on discharge. There is little or no change in the intensity of the 1s-3d transition during cycles **A** and **B**. This provides direct evidence that the vanadium remains in an approximately octahedral environment during electrochemical cycling to 4.5 V. In sharp contrast, the 1s-3d intensity more than doubles when the potential is raised to 4.8 V, (Figure 4c,d) and this increase is not fully reversed during the reductive half of the cycle. This increase in 1s-3d intensity is consistent with a distorted vanadium environment. The EXAFS data give a similar picture. In all

cases (see Figure S7) samples show the V-O nearest neighbor and V•••P and V•••O outer shell scattering expected from the crystal structure of $Li_3V_2(PO_4)_3$. This confirms the absence of detectable vanadium impurities. There is no significant change in this structure for cycles **A**-**C**, consistent with retention of the structure throughout charge and discharge.[8-15] However, there are significant, reversible changes in the average V-O nearest neighbor distance during each cycle (see Table S2) consistent with oxidation and reduction of the vanadium ions. For cycle **D** there is a noticeable splitting in the outer shell scattering, suggesting a change in the longer-range order.

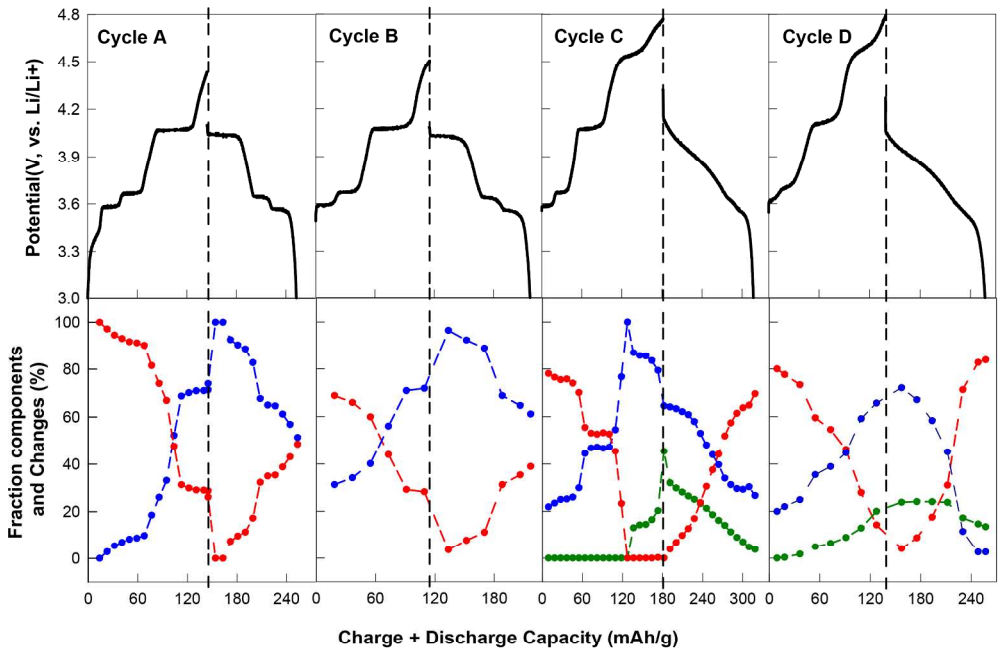

Figure 2. Charge-discharge profiles 0.1 C (**A** and **C**) and 0.2 C (**B** and **D**) (upper panel); the composition of the PCA components (lower panel) 1 (red dots), 2 (blue dots) 3 (green dots)

XAS is a bulk method, giving the average spectrum for a mixture that could, in principle, contain many different components. To analyze the data, we first used principal component analysis (PCA)[41] to determine the number of unique components that are required to account for the observed data. For both cycles **A** and **B**, only two components are necessary to fit the data; for cycles **C** and **D** a third component is required (Figure S2).

A well-known difficulty with PCA is that while it is useful for determining the number of components, determining the spectra for these components typically requires additional information. We used Iterative Target Factor Analysis (ITFA)[23] to estimate the true component spectra. The spectra for cycles **A** and **B** were analyzed as a group; with the only hard constraint being that Component 1 was 100% at the start of charge cycle A. In addition, Components 1 and 2 were constrained to be between 0 and 100% at the start of the first discharge. Spectra for cycles **C** and **D** were analyzed similarly, with the constraints for Component 1 defined by the edge energy (see below): 69% Component 1 at the start of **C** and 80% at the start of **D**. Component 3 was fixed at 0% at the start of the first charge, and stable refinements required the additional constraint that component 2 was > 10% at the beginning of the discharge for cycle **C**. The resulting component spectra are shown in Figure 1 and the calculated charge compositions in Figure 2. The calculated spectra for Components 1 and 2 (Figure 1) are similar to authentic spectra for V^{3+} and V^{4+}, consistent with the expected electrochemistry. The near identity of the Component 1 and 2 spectra that are calculated using different data sets gives us demonstrates that this is a robust, stable solution, and gives us confidence using these components for further analysis.

With the availability of quantitative composition analysis for each spectrum, we are in a unique position to characterize the oxidation-state evolution of the cathode. For cycle **A**, the

amount of component 1 is largely unchanged until ~50 mAh g^{-1}, (see Figure 2) at which point it decreases until ~100 mAh g^{-1}. After this the conversion largely stops, with no significant additional change until the beginning of the discharge portion of cycle **A**. Similar discontinuities are seen on discharge. Results for cycles **B**-**D** are very similar, albeit from a different starting composition and, for **C** and **D**, with the addition of Component 3. For **C** and **D**, full oxidation to V^{4+} does not take place until the potential reaches ~4.5 V; above 4.5 V Component 3 is formed. The discontinuities are less pronounced for **B** and **D**, consistent with the higher current in these cycles.

As an alternative approach, independent of PCA, the data were also fit using authentic V^{3+} and V^{4+} reference spectra (Figure S8). These fits (Figure S3) are analogous to fits using the spectra from Figure 1, but allow an independent estimate of the average oxidation state. The results confirm Figure 2: ~100% V^{3+} at the start of **A**, with oxidation to $V^{3.75+}$ by 100 mAh g^{-1} but little further change over the 4.0 V plateau and full oxidation to V^{4+} only after the sample has equilibrated for ~ 1 h at 4.5 V. The average vanadium oxidation states as determined from these fits are given in Table S3; these were used as constraints for the amount of the V^{3+} that was present at the start of each oxidative cycle during the ITFA analysis for cycles **C** and **D**.

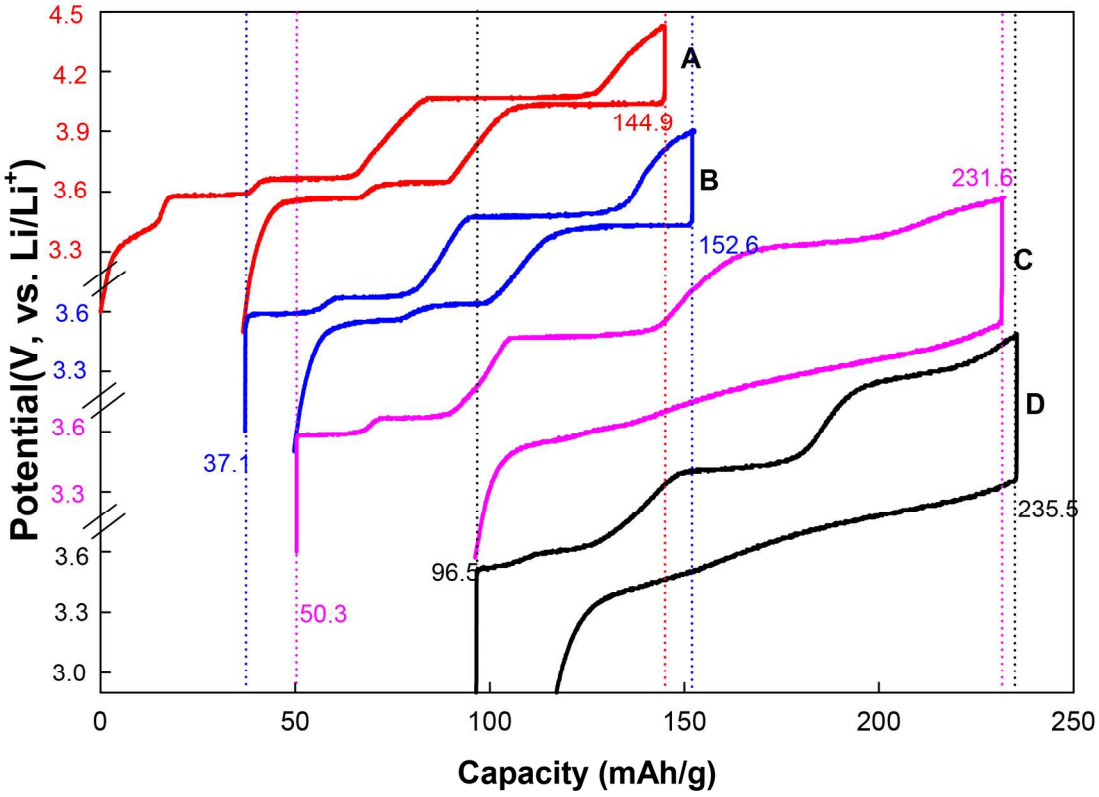

Figure 3. Charge-discharge profiles for $Li_3V_2(PO_4)_3$ at 0.1 C (**A** and **C**), and 0.2 C (**B** and **D**). **A** & **B** are from 3 – 4.5 V; **C** & **D** from 3 – 4.8 V. Successive cycles are offset vertically for clarity as indicated on the y-scale. The dotted line are guide to the eye, shows the start of charge and the end of discharge for each cycle and the labels show the corresponding capacities.

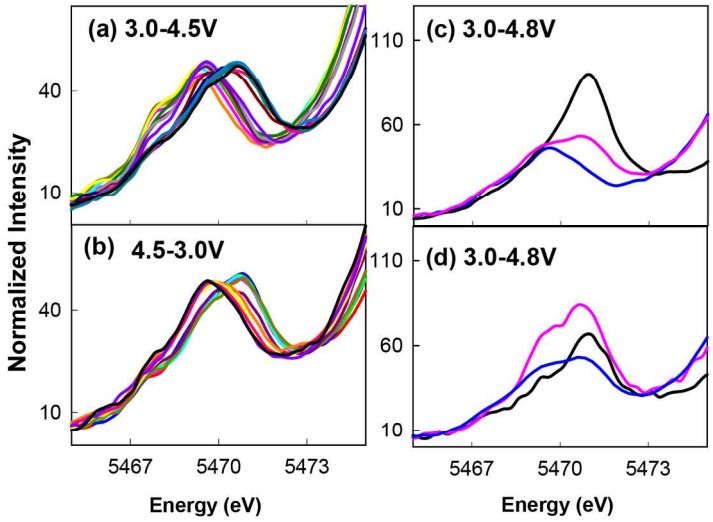

Figure 4. a) and b) 1s-3d transitions for the data in Figure S6 for cycle **A**; c) and d) 1s-3d transitions for cycles **C** and **D**. (Figure S6) Initial charge spectrum (3.0 V) is blue line; 4.8 V spectrum is black; final discharge spectrum (3.0 V) is pink line.

In addition to these quantitative approaches to the data, we also explored two phenomenological comparisons. The total change in edge energy (judged as the energy at 650 $cm^2\ g^{-1}$) is 1.74 eV (for charge), 1.26 eV (for discharge) in cycle **A**. From this, we can calculate the fractional change in edge energy for each successive scan. Similarly, we calculated the fractional change in bond-length during each charge and discharge cycle. These model-independent approaches (Figure S3) confirm the strikingly non-linear redox behavior illustrated in Figure 2.

The availability of capacity-dependent average oxidation states (Figure 2) provides a unique opportunity to characterize the behavior of the electrode in detail. We find (Table S4) excellent agreement between the observed capacity and the measured change in vanadium oxidation state. While it is possible that there are some side reactions during cycles **A** and **B**, perhaps as the

result of SEI formation, we find that most of the capacity loss that is seen in Figure 3 can be explained by incomplete vanadium reduction.

Discussion

Our analysis procedure has allowed us to define the evolution of vanadium oxidation state as a function of the state of charge. Perhaps the most surprising observation to come from this work is the finding that well-defined electrochemical transitions are not well correlated with bulk vanadium oxidation state for these samples. The plateaus at 3.6 and 3.7 V, attributed to $V^{3+} \leftrightarrows V^{3.25+}$ and $V^{3.25+} \leftrightarrows V^{3.5+}$, respectively, are seen to correspond to only a small change in the average vanadium oxidation state. By the start of the 4 V plateau, attributed to $V^{3.5+} \leftrightarrows V^{4+}$, about 20-30% of the vanadium has been oxidized, as determined either from PCA/ITFA or from fits with authentic V^{3+} and V^{4+}. This is less oxidized than would be expected for the nominal $V^{3.5+}$ structure, but this changes rapidly during the first part of the 4 V plateau, where the average oxidation state increases rapidly to the point that ~70% of the V^{3+} has been oxidized to V^{4+}, after which the oxidation state stabilizes with little further oxidation during the rest of the 4 V plateau.

The electrochemical measurements demonstrate that our samples are electrochemically homogeneous; if there were spatial heterogeneities such as those seen during oxidation of $LiFePO_4$[40] we would expect to see broader, less well defined steps and plateaus in Figure 3. We attribute our observations to slow mass transport of Li in the individual $Li_3V_2(PO_4)_3$ particles, perhaps through a mechanism similar to that described recently for NiO[42]. Our data thus reflect the fact that the electrochemical measurements reflect only the state of the vanadium ions on the surface of the $Li_3V_2(PO_4)_3$ particles, while XAS is sensitive to all of the vanadium in the sample. An analogous surface-bulk heterogeneity was seen recently in $LiFePO_4$,[43] using x-ray microprobe imaging. It is intriguing that there appears to be a change in redox rate at ~3.6 V on

both the oxidative and the reductive cycles. It may be that the $LiV_2(PO_4)_3$ surface structure, which begins forming at approximately 3.6 V, is more conducive to Li transport from the bulk, and formation of this structure allows the bulk composition to "catch up" to the surface.[44]

Further evidence of a difference between surface and bulk composition is found in the fact that both the potential and the average vanadium oxidation state continue to change during the ~ 1 hour that elapsed between the end of a charge and the beginning of a discharge cycle, and between the end of the discharge and the beginning of the next charge, despite the absence of current flow (see Figures 3 and 2). The potential drops by 0.4-0.6 V on sitting after a charge cycle and increases by ~0.6 V on sitting after a discharge cycle. Similarly, the vanadium is not fully oxidized by the end of the oxidative half of the cycle and it is only after the cathode has been allowed to equilibrate without current flow for ~ 1 hr that we see full formation of V^{4+}. The same thing happens at low potential. The average vanadium oxidation state (see Table S3) is 3.6 at the end of the first discharge but 3.3 at the start of the second charge. Time-dependent XANES spectra measured during this equilibration period (Figure S4) capture this recovery in vanadium oxidation state directly; this can be modeled as an exponential relaxation with a time constant of 0.02-0.08 min^{-1}. Recovery at this rate may account for the lack of a lag phase in an earlier *in situ* study at 50% slower rate of charge.[26]

These observations suggest that, at least for our samples, charge can be stored on a non-vanadium site, perhaps via a capacitive mechanism[45-46] during the slow oxidation/reduction phases (e.g. 0-60 mAh g^{-1}) and delivered to vanadium during the more rapid phases (e.g., 50-100 mAh g^{-1}). An interesting corollary of these results is that they suggest an alternative explanation for the observed hysteresis. Earlier work, using chemically-prepared $Li_xV_2(PO_4)_3$ (x=0,1,2,3) attributed the hysteresis to the presence of oxidation state ordering.[8] Our data suggests a simpler

explanation. The hysteresis in our measurements may be the result of equilibration of the bulk material with the surface, such that the electrochemically active surface sites are different at the start of the reductive cycle than they were at the end of the oxidative cycle.

This behavior can be summarized in a Faraday's law plot. The theoretical capacity is 131 mAh g^{-1} for each unit change in average oxidation state. The actual average vanadium oxidation state can be calculated from the fitted composition (Figure 2), assigning Component 1 as V^{3+}, Component 2 as V^{4+}, and Component 3 as V^{5+}. The expected and observed electrochemical behavior are compared in Figure 5, showing clearly that there are significant deviations from Faraday's law due to the lag for surface to bulk equilibration. For charging up to approximately 100 mAh g^{-1} there is less oxidation than expected, followed by faster than expected oxidation.

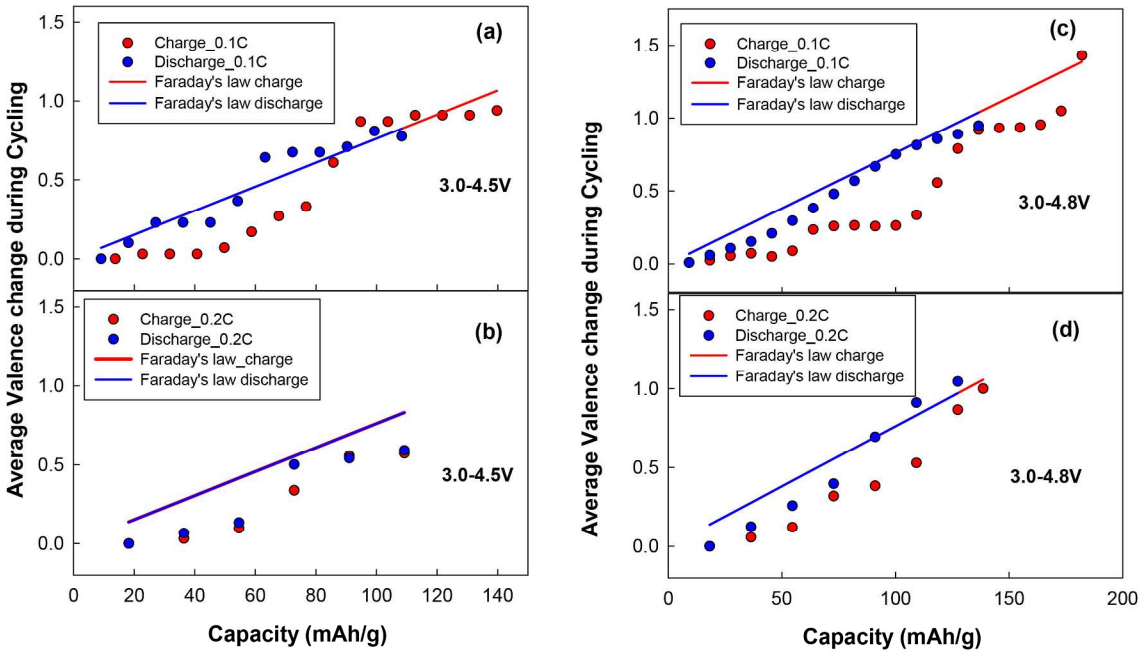

Figure 5. Comparison of the Faraday's law prediction of the average valence with the observed average valence for each of the 4 cycles. Solid lines are the predicted average valence, using the theoretical capacity as mentioned in text. Circles are the calculated average valence from the

XAS data. (a), (b) 3-4.5 V at 0.1C and 0.2C rates; (c), (d) 3-4.8V at 0.1C and 0.2C rates. Red lines and points represent charging; blue represent discharge

Finally, in addition to the kinetic lag, we have discovered that when the potential is raised above 4.5 V there is a significant change in the vanadium environment. The weak 1s-3d transition that is observed for spectra in cycles **A** and **B** is consistent with the distorted VO_6 octahedra found in monoclinic LVP.[9] The dramatic increase in 1s-3d intensity when the potential exceeds 4.5 V provides unambiguous evidence of a significant perturbation in vanadium structure. This phenomenon is qualitatively similar to that seen, but not interpreted in earlier studies.[40, 47] Our ability to isolate spectra for Component 3 (i.e., Figure 1) provides clear evidence for formation of a new structure above 4.5 V. One explanation for the increase would be formation of a strongly covalent vanadyl-like species;[48-49] however, formation of such a species seems unlikely since it would require decomposition of the phosphate backbone. Alternatively, a change in vanadium geometry could account for the change in 1s-3d intensity, since tetrahedral metal sites have significantly more intense 1s-3d transitions due to the possibility of *d*+*p* orbital mixing in non-centrosymmetric environments. This could happen through anti-site mixing, with a portion, perhaps 10-20% (see Table S1), of the vanadium migrating to one of the now-empty Li sites. These[9] are tetrahedral, Li(1); and five-coordinate, Li(2) and Li(3), and would thus be expected to give greatly enhanced 1s-3d intensities. Further evidence of migration is seen in the EXAFS, where for cycles **C** and **D** there is a noticeable splitting in the outer shell scattering at high potential (Figure S7); this might arise if there were a mixture of larger O_h and smaller T_d vanadium sites. Anti-site mixing has not been proposed

previously[8], perhaps due to the lower sensitivity of diffraction measurements to small amounts mixing.

The observation that this putative migration only occurs above 4.5 V is consistent with the finding that only above 4.5 V is the smaller V^{5+} cation formed. It appears that, at least under our conditions, this migration is partially reversible, after we allow time for the electrode to equilibrate (peak areas are given in Table S1). At the end of cycle **D**, the 1s-3d amplitude remains enhanced, consistent with some vanadium remaining in a tetrahedral site, although this may reflect the fact that the electrode was not allowed to equilibrate at the end of **D**. Occupation of some of the Li sites by vanadium would provide an atomic-level explanation for the capacity loss that is found when LVP electrodes are cycled above 4.5 V. A key practical question for future studies will be whether this putative migration can be prevented, which would allow utilization of LVP over a wider potential range, or if not prevented, than at least repaired. The observation that the 1s-3d amplitude can be reduced by ~1 hour at 3 V suggests that electron injection may eliminate anti-site mixing, as seen previously in $LiFePO_4$.[23]

Conclusions

From *in situ* continuous XAS measurements, we have demonstrated that vanadium oxidation in $Li_3V_2(PO_4)_3$ as detected electrochemically is uncoupled from bulk oxidation state. We interpret this as reflecting a significant kinetic lag between the surface electrochemistry and the bulk vanadium composition. We find that only ~20-30% of the vanadium has been oxidized at the start of the nominal $V^{3.5+} \leftrightarrow V^{4+}$ transition, in contrast with the 50% that would be expected from the electrochemistry. The presence of this lag has implications both for the interpretation of electrochemical measurements and for the optimization of electrode performance. Secondly, we show for the first time that the capacity loss that occurs when $Li_3V_2(PO_4)_3$ electrodes are raised

above ~4.5 volts results from formation of a novel, distorted vanadium site, consistent with tetrahedral vanadium. We interpret this as resulting from Li-V anti-site mixing. This has important implications for understanding the stability of this class of electrode materials.

Supporting Information. Detail of sample characterization, XANES spectra for cycles B-D, PCA analysis, EXAFS spectra, and fitting details.

Corresponding Authors

*E-mail: jeph@umich.edu (JEPH); debani@umich.edu (AD)

Author Contributions

ZZ, SW, and LY prepared the electrode materials and performed XRD and SEM characterization. SK, AD, and JEPH measured the XAS data. SK and AD analyzed the XAS data, and with JEPH and EC interpreted the data. SK, AD, JEPH, LY, and EC contributed to writing the paper. All authors have given approval to the final version of the manuscript.

ACKNOWLEDGMENT

Financial support for this work came from a University of Michigan–Shanghai Jiao Tong University collaborative research project. Li Yang acknowledges the National Natural Science Foundation of China (Grants No. 21103108 and 21173148).DND-CAT (5-BM-D) is supported by the E.I. DuPont de Nemours and Co., The Dow Chemical Company, the U.S. NSF through Grant DMR-9304725, and State of Illinois, Department of Commerce and the Board of Higher Education Grant IBHEHECANWU96.

REFERENCES

1. Chen, J.; Wang, S.; Whittingham, M. S., Hydrothermal synthesis of cathode materials. *J. Power Sources* **2007**, *174*, 442-448.
2. Wang, D. Y.; Buqa, H.; Crouzet, M.; Deghenghi, G.; Drezen, T.; Exnar, I.; Kwon, N. H.; Miners, J. H.; Poletto, L.; Graetzel, M., High-performance, nano-structured $LiMnPO_4$ synthesized via a polyol method. *J. Power Sources* **2009**, *189*, 624-628.
3. Padhi, A. K.; Nanjundaswamy, K. S.; Goodenough, J. B., Phospho-olivines as positive-electrode materials for rechargeable lithium batteries. *J. Electrochem. Soc.* **1997**, *144*, 1188-1194.
4. Zhou, F.; Cococcioni, M.; Kang, K.; Ceder, G., The Li intercalation potential of $LiMPO_4$ and $LiMSiO_4$ olivines with M = Fe, Mn, Co, Ni. *Electrochem. Commun.* **2004**, *6*, 1144-1148.
5. Wang, L.; Zhang, L. C.; Lieberwirth, I.; Xu, H. W.; Chen, C. H., A $Li_3V_2(PO_4)_3$/C thin film with high rate capability as a cathode material for lithium-ion batteries. *Electrochem. Commun.* **2010**, *12*, 52-55.
6. Huang, H.; Faulkner, T.; Barker, J.; Saidi, M. Y., Lithium metal phosphates, power and automotive applications. *J. Power Sources* **2009**, *189*, 748-751.
7. Gaubicher, J.; Wurm, C.; Goward, G.; Masquelier, C.; Nazar, L., Rhombohedral form of $Li_3V_2(PO_4)_3$ as a cathode in Li-ion batteries. *Chem. Mater.* **2000**, *12*, 3240-+.
8. Yin, S. C.; Grondey, H.; Strobel, P.; Anne, M.; Nazar, L. F., Electrochemical property: Structure relationships in monoclinic $Li_{3-y}V_2(PO_4)_3$. *J. Am. Chem. Soc.* **2003**, *125*, 10402-10411.
9. Yin, S. C.; Grondey, H.; Strobel, P.; Huang, H.; Nazar, L. F., Charge ordering in lithium vanadium phosphates: Electrode materials for lithium-ion batteries. *J. Am. Chem. Soc.* **2003**, *125*, 326-327.
10. Sato, M.; Ohkawa, H.; Yoshida, K.; Saito, M.; Uematsu, K.; Toda, K., Enhancement of discharge capacity of $Li_3V_2(PO_4)_3$ by stabilizing the orthorhombic phase at room temperature. *Solid State Ionics* **2000**, *135*, 137-142.
11. Morgan, D.; Ceder, G.; Saidi, M. Y.; Barker, J.; Swoyer, J.; Huang, H.; Adamson, G., Experimental and computational study of the structure and electrochemical properties of

$Li_xM_2(PO_4)_3$ compounds with the monoclinic and rhombohedral structure. *Chem. Mater.* **2002**, *14*, 4684-4693.

12. Barker, J.; Gover, R. K. B.; Burns, P.; Bryan, A., The effect of Al substitution on the electrochemical insertion properties of the lithium vanadium phosphate, $Li_3V_2(PO_4)_3$. *J. Electrochem. Soc.* **2007**, *154*, A307-A313.
13. Barker, J.; Gover, R. K. B.; Burns, P.; Bryan, A. J., $Li_{4/3}Ti_{5/3}O_4$ parallel to $Na_3V_2(PO_4)_2F_3$: An example of a hybrid-ion cell using a non-graphitic anode. *J. Electrochem. Soc.* **2007**, *154*, A882-A887.
14. Barker, J.; Gover, R. K. B.; Burns, P.; Bryan, A. J., A lithium-ion cell based on $L_{i4/3}T_{i5/3}O_4$ and $LiVPO_4F$. *Electrochem. Solid-State Lett.* **2007**, *10*, A130-A133.
15. Saidi, M. Y.; Barker, J.; Huang, H.; Swoyer, J. L.; Adamson, G., Electrochemical properties of lithium vanadium phosphate as a cathode material for lithium-ion batteries. *Electrochem. Solid-State Lett.* **2002**, *5*, A149-A151.
16. Huang, J. S.; Yang, L.; Liu, K. Y.; Tang, Y. F., Synthesis and characterization of $Li_3V_{2-2x/3}Mg_x(PO_4)_3$/C cathode material for lithium-ion batteries. *J. Power Sources* **2010**, *195*, 5013-5018.
17. Deb, A.; Bergmann, U.; Cairns, E. J.; Cramer, S. P., X-ray absorption spectroscopy study of the LixFePO4 cathode during cycling using a novel electrochemical in situ reaction cell. *J. Synchrotron. Radiat.* **2004**, *11*, 497-504.
18. Weng, T. C.; Waldo, G. S.; Penner-Hahn, J. E., A method for normalization of X-ray absorption spectra. *J. Synchrotron. Radiat.* **2005**, *12*, 506-510.
19. George G.N., P. I. J., Exafspak, Stanford Synchrotron Radiation Laboratory, Stanford, CA. In *Exafspak, Stanford Synchrotron Radiation Laboratory, Stanford, CA*, 1993.
20. Rehr, J. J.; Kas, J. J.; Vila, F. D.; Prange, M. P.; Jorissen, K., Parameter-free calculations of X-ray spectra with FEFF9. *Phys. Chem. Chem. Phys.* **2010**, *12*, 5503-5513.
21. Victoreen, J. A., The Absorption of Incident Quanta by Atoms as Defined by the Mass Photoelectric Absorption Coefficient and the Mass Scattering Coefficient. *J. Appl. Phys.* **1948**, *19*, 855-860.
22. PRESTOPRONTO, Version b0.670. http://www.esrf.eu/computing/scientific/PRESTOPRONTO/Prestopronto.htm (accessed February 25, 2016).
23. Park, K.-Y.; Park, I.; Kim, H.; Lim, H.-d.; Hong, J.; Kim, J.; Kang, K., Anti-Site Reordering in LiFePO4: Defect Annihilation on Charge Carrier Injection. *Chem. Mater.* **2014**, *26*, 5345-5351.
24. Webb, S. M., SIXpack: a graphical user interface for XAS analysis using IFEFFIT. *Phys. Scr.* **2005**, *2005*, 1011.
25. Newville, M., IFEFFIT: interactive XAFS analysis and FEFF fitting. *J. Synchrotron. Radiat.* **2001**, *8*, 322-324.
26. Pivko, M.; Arcon, I.; Bele, M.; Dominko, R.; Gaberscek, M., $A_3V_2(PO_4)_3$ (A = Na or Li) probed by in situ X-ray absorption spectroscopy. *J. Power Sources* **2012**, *216*, 145-151.
27. Cho, A. R.; Son, J. N.; Aravindan, V.; Kim, H.; Kang, K. S.; Yoon, W. S.; Kim, W. S.; Lee, Y. S., Carbon supported, Al doped-$Li_3V_2(PO_4)_3$ as a high rate cathode material for lithium-ion batteries. *J. Mater. Chem.* **2012**, *22*, 6556-6560.
28. Yang, G.; Ji, H. M.; Liu, H. D.; Qian, B.; Jiang, X. F., Crystal structure and electrochemical performance of $Li_3V_2(PO_4)_3$ synthesized by optimized microwave solid-state synthesis route. *Electrochim. Acta* **2010**, *55*, 3669-3680.

29. Qiao, Y. Q.; Wang, X. L.; Xiang, J. Y.; Zhang, D.; Liu, W. L.; Tu, J. P., Electrochemical performance of $Li_3V_2(PO_4)_3$/C cathode materials using stearic acid as a carbon source. *Electrochim. Acta* **2011**, *56*, 2269-2275.
30. Chen, Q. Q.; Wang, J. M.; Tang, Z.; He, W. C.; Shao, H. B.; Zhang, J. Q., Electrochemical performance of the carbon coated $Li_3V_2(PO_4)_3$ cathode material synthesized by a sol-gel method. *Electrochim. Acta* **2007**, *52*, 5251-5257.
31. Wang, W. H.; Zhang, J. L.; Jia, Z.; Dai, C. S.; Hu, Y. F.; Zhou, J. G.; Xiao, Q. F., Enhancement of the cycling performance of$Li_3V_2(PO_4)_3$/C by stabilizing the crystal structure through Zn^{2+} doping. *Phys. Chem. Chem. Phys.* **2014**, *16*, 13858-13865.
32. Wang, C.; Liu, H. M.; Yang, W. S., An integrated core-shell structured$Li_3V_2(PO_4)_3$@C cathode material of LIBs prepared by a momentary freeze-drying method. *J. Mater. Chem.* **2012**, *22*, 5281-5285.
33. Liu, H. D.; Yang, G.; Zhang, X. F.; Gao, P.; Wang, L.; Fang, J. H.; Pinto, J.; Jiang, X. F., Kinetics of conventional carbon coated-$Li_3V_2(PO_4)_3$ and nanocomposite $Li_3V_2(PO_4)_3$/graphene as cathode materials for lithium ion batteries. *J. Mater. Chem.* **2012**, *22*, 11039-11047.
34. Wei, Q. L.; An, Q. Y.; Chen, D. D.; Mai, L. Q.; Chen, S. Y.; Zhao, Y. L.; Hercule, K. M.; Xu, L.; Minhas-Khan, A.; Zhang, Q. J., One-Pot Synthesized Bicontinuous Hierarchical $Li_3V_2(PO_4)_3$/C Mesoporous Nanowires for High-Rate and Ultralong-Life Lithium-ion Batteries. *Nano Lett.* **2014**, *14*, 1042-1048.
35. Saidi, M. Y.; Barker, J.; Huang, H.; Swoyer, J. L.; Adamson, G., Performance characteristics of lithium vanadium phosphate as a cathode material for lithium-ion batteries. *J. Power Sources* **2003**, *119*, 266-272.
36. Zhang, L.; Wang, X. L.; Xiang, J. Y.; Zhou, Y.; Shi, S. J.; Tu, J. P., Synthesis and electrochemical performances of $Li_3V_2(PO_4)_3$/(Ag + C) composite cathode. *J. Power Sources* **2010**, *195*, 5057-5061.
37. Du, X. Y.; He, W.; Zhang, X. D.; Yue, Y. Z.; Liu, H.; Zhang, X. G.; Min, D. D.; Ge, X. X.; Du, Y., Enhancing the electrochemical performance of lithium ion batteries using mesoporous $Li_3V_2(PO_4)_3$/C microspheres. *J. Mater. Chem.* **2012**, *22*, 5960-5969.
38. Chen, Y. H.; Zhao, Y. M.; An, X. N.; Liu, J. M.; Dong, Y. Z.; Chen, L., Preparation and electrochemical performance studies on Cr-doped $Li_3V_2(PO_4)_3$ as cathode materials for lithium-ion batteries. *Electrochim. Acta* **2009**, *54*, 5844-5850.
39. Ren, M. M.; Zhou, Z.; Li, Y. Z.; Gao, X. P.; Yan, J., Preparation and electrochemical studies of Fe-doped $Li_3V_2(PO_4)_3$ cathode materials for lithium-ion batteries. *J. Power Sources* **2006**, *162*, 1357-1362.
40. Strobridge, F. C., et al., Mapping the Inhomogeneous Electrochemical Reaction Through Porous LiFePO4-Electrodes in a Standard Coin Cell Battery. *Chem. Mater.* **2015**, *27*, 2374-2386.
41. Manceau, A.; Marcus, M.; Lenoir, T., Estimating the number of pure chemical components in a mixture by X-ray absorption spectroscopy. *J. Synchrotron. Radiat.* **2014**, *21*, 1140-1147.
42. He, K., et al., Transitions from Near-Surface to Interior Redox upon Lithiation in Conversion Electrode Materials. *Nano Lett.* **2015**, *15*, 1437-1444.
43. Wang, X.-J.; Jaye, C.; Nam, K.-W.; Zhang, B.; Chen, H.-Y.; Bai, J.; Li, H.; Huang, X.; Fischer, D. A.; Yang, X.-Q., Investigation of the structural changes in Li1-xFePO4 upon charging by synchrotron radiation techniques. *J. Mater. Chem.* **2011**, *21*, 11406-11411.

44. Han, D.-W.; Lim, S.-J.; Kim, Y.-I.; Kang, S. H.; Lee, Y. C.; Kang, Y.-M., Facile Lithium Ion Transport through Superionic Pathways Formed on the Surface of $Li_3V_2(PO_4)_3$/C for High Power Li Ion Battery. *Chem. Mater.* **2014**, *26*, 3644-3650.
45. Secchiaroli, M.; Giuli, G.; Fuchs, B.; Marassi, R.; Wohlfahrt-Mehrens, M.; Dsoke, S., High rate capability $Li_3V_{2-x}Ni_x(PO_4)_3$/C (x = 0, 0.05, and 0.1) cathodes for Li-ion asymmetric supercapacitors. *J. Mater. Chem. A* **2015**, *3*, 11807-11816.
46. Satish, R.; Aravindan, V.; Ling, W. C.; Madhavi, S., Carbon-coated $Li_3V_2(PO_4)_3$ as insertion type electrode for lithium-ion hybrid electrochemical capacitors: An evaluation of anode and cathodic performance. *J. Power Sources* **2015**, *281*, 310-317.
47. Yoon, J.; Muhammad, S.; Jang, D.; Sivakumar, N.; Kim, J.; Jang, W.-H.; Lee, Y.-S.; Park, Y.-U.; Kang, K.; Yoon, W.-S., Study on structure and electrochemical properties of carbon-coated monoclinic $Li_3V_2(PO_4)_3$ using synchrotron based in situ X-ray diffraction and absorption. *J. Alloys Compd.* **2013**, *569*, 76-81.
48. Wong, J.; Lytle, F. W.; Messmer, R. P.; Maylotte, D. H., K-Edge Absorption-Spectra of Selected Vanadium Compounds. *Phys. Rev. B* **1984**, *30*, 5596-5610.
49. Allen, C. J.; Jia, Q.; Chinnasamy, C. N.; Mukerjee, S.; Abraham, K. M., Synthesis, Structure and Electrochemistry of Lithium Vanadium Phosphate Cathode Materials. *J. Electrochem. Soc.* **2011**, *158*, A1250-A1259.

Table of Contents Graphic:

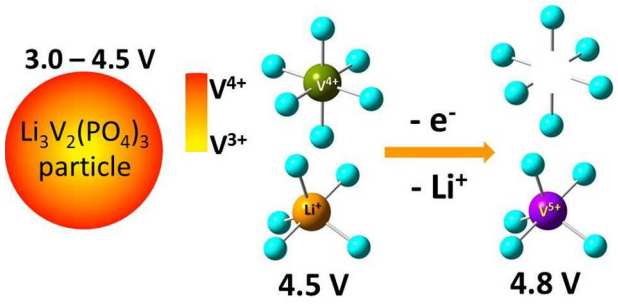

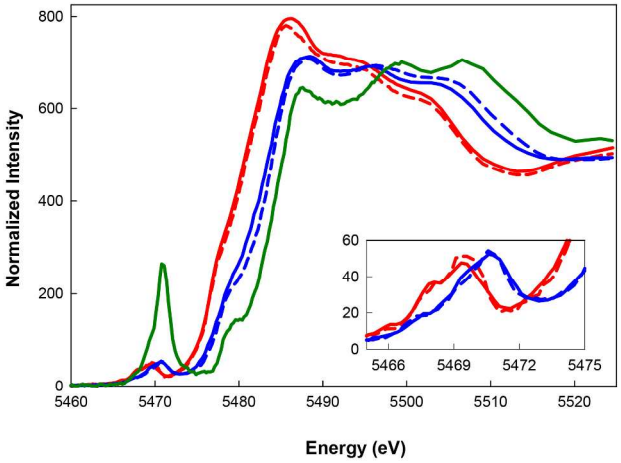

Figure 1. ITFA reconstructed components. Red) Component 1 for **A**, **B**, (solid) and **C**, **D** (dashed); Blue) Component 2 for **A**, **B** (solid) and **C**, **D** (dashed); Green) Component 3 for **C** and **D**
215x279mm (300 x 300 DPI)

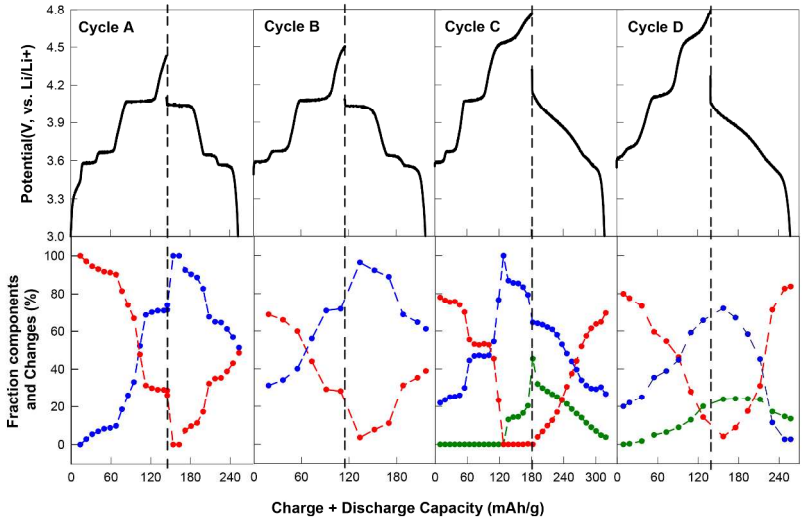

Figure 2. Charge-discharge profiles 0.1 C **(A** and **C**) and 0.2 C (**B** and **D**) (upper panel); the composition of the PCA components (lower panel) 1 (red dots), 2 (blue dots) 3 (green dots)
279x215mm (300 x 300 DPI)

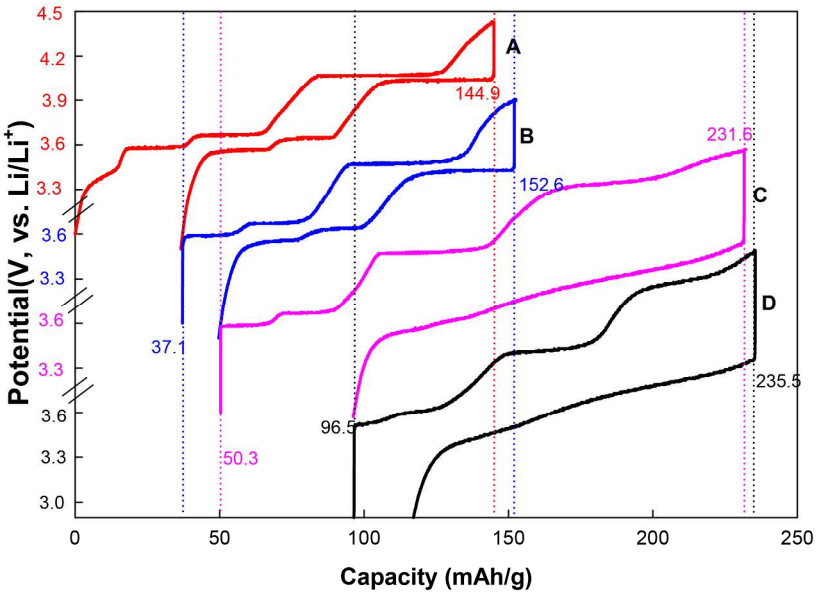

Figure 3. Charge-discharge profiles for $Li_3V_2(PO_4)_3$ at 0.1 C (**A** and **C**), and 0.2 C (**B** and D). **A** & **B** are from 3 – 4.5 V; **C** & **D** from 3 – 4.8 V. Successive cycles are offset vertically for clarity as indicated on the y-scale. The dotted line are guide to the eye, shows the start of charge and the end of discharge for each cycle and the labels show the corresponding capacities.
215x279mm (300 x 300 DPI)

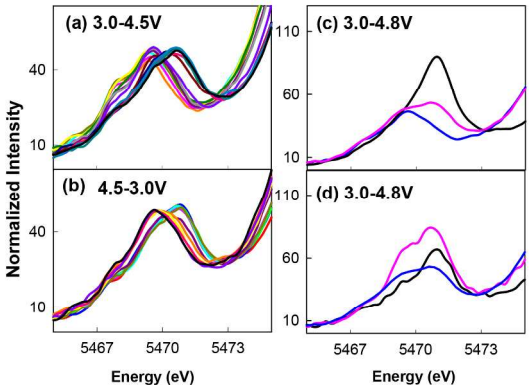

Figure 4. a) and b) 1s-3d transitions for the data in Figure S3 for cycle **A**; c) and d) 1s-3d transitions for cycles **C** and **D**. (Figure S3) Initial charge spectrum (3.0 V) is blue line; 4.8 V spectrum is black; final discharge spectrum (3.0 V) is pink line.
215x279mm (300 x 300 DPI)

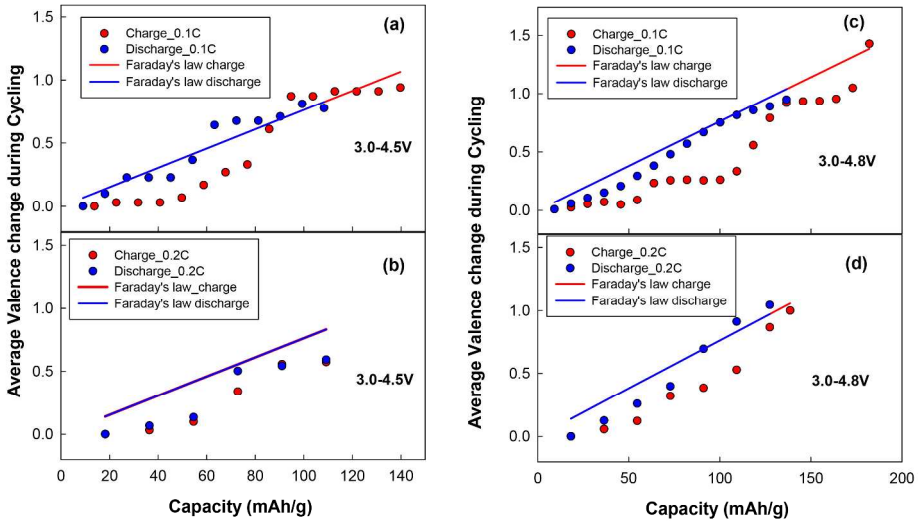

Figure 5. Comparison of the Faraday's law prediction of the average valence with the observed average valence for each of the 4 cycles. Solid lines are the predicted average valence, using the theoretical capacity as mentioned in text. Circles are the calculated average valence from the XAS data. (a), (b) 3-4.5 V at 0.1C and 0.2C rates; (c), (d) 3-4.8V at 0.1C and 0.2C rates. Red lines and points represent charging; blue represent discharge
279x215mm (300 x 300 DPI)